

Double aberration correction in a low-energy electron microscope

Th. Schmidt^{a,b,*}, H. Marchetto^a, P.L. Lévesque^a, U. Groh^b, F. Maier^b, D. Preikszas^{c,f}, P. Hartel^{c,1}, R. Spehr^c, G. Lilienkamp^e, W. Engel^a, R. Fink^d, E. Bauer^{e,g}, H. Rose^c, E. Umbach^b, H.-J. Freund^a

^a Fritz-Haber-Institut der Max-Planck-Gesellschaft, Faradayweg 6-8, D-14195 Berlin, Germany

^b Universität Würzburg, Experimentelle Physik II, Am Hubland, D-97074 Würzburg, Germany

^c Technische Universität Darmstadt, Angewandte Physik, Hochschulstraße 6, D-64289 Darmstadt, Germany

^d Universität Erlangen-Nürnberg, Physikalische Chemie II, Egerlandstraße 3, D-91058 Erlangen, Germany

^e Technische Universität Clausthal, Physikalisches Institut, Leibnizstraße 4, D-38678, Germany

^f Carl Zeiss NTS GmbH, Carl-Zeiss-Straße 56, D-73447 Oberkochen, Germany

^g Arizona State University, Department of Physics, Tempe, AZ 85287, USA

ARTICLE INFO

Article history:

Received 4 February 2010

Received in revised form

22 June 2010

Accepted 8 July 2010

Keywords:

Aberration correction

Low-energy electron microscopy

High resolution electron microscopy

ABSTRACT

The lateral resolution of a surface sensitive low-energy electron microscope (LEEM) has been improved below 4 nm for the first time. This breakthrough has only been possible by simultaneously correcting the unavoidable spherical and chromatic aberrations of the lens system. We present an experimental criterion to quantify the aberration correction and to optimize the electron optical system. The obtained lateral resolution of 2.6 nm in LEEM enables the first surface sensitive, electron microscopic observation of the herringbone reconstruction on the Au(1 1 1) surface.

© 2010 Elsevier B.V. All rights reserved.

1. Introduction

Cathode lens electron microscopes like LEEM or (X-ray) photoelectron emission microscopes (X-PEEM) have attracted an increasing interest in surface science over the last two decades [1–3]. The high surface sensitivity, the possibility for in-situ and real-time investigation under ultra-high vacuum conditions, the various image contrast mechanisms and the combination of pure microscopy with diffraction and spectroscopic methods [4] are the main reasons that these microscopes are applied in many areas of surface physics, chemistry or nanotechnology. Examples are the crystal growth of atomic or molecular layers [5,6], phase transitions [7], surface magnetism [8–10] or chemical reactions [11]. Up to now, the size for the investigated objects ranges from a few micrometers down to the present resolution limit of 4–5 nm (LEEM) or 22 nm (XPEEM)[4]. Expanding this range beyond this limit allows to investigate, for instance, the chemical composition of individual nanometer sized particles. Unfortunately, a fundamental barrier hinders the resolution improvement of these cathode lens microscopes. Unlike in light optics, where aberrations of a lens system can be compensated by a simple combination of convex and concave lenses, this is not possible

* Corresponding author at: Fritz-Haber-Institut, Department of Chemical Physics, Faradayweg

4-6, D-14195 Berlin, Germany, Tel.: +49 30 8062 1 4671; fax: +49 30 8413 4101.

E-mail address: schmidtth@fhi-berlin.mpg.de (Th. Schmidt).

¹ Present address: CEOS GmbH, Englerstr. 28, D-69126, Heidelberg, Germany.

in electron optics. Therefore, since invention of electron microscopy in the 1930s the aberrations of electron lenses have only been reduced by optimizing the geometric design, increasing the electron energy and using magnetic instead of electrostatic fields, but the resolution limiting aberrations could not be eliminated. Already in 1936 Scherzer [12] stated that *chromatic and spherical aberrations of static round lenses are unavoidable in the absence of space charge and flight reversal*. Various methods, suggested or already employed in electron microscopes compensate aberrations by circumventing [13,14] one of the above mentioned constraints. In transmission electron microscopes (TEM) Haider et al. compensate for the spherical aberration by a multipole corrector [15], resulting in a lateral resolution better than 0.1 nm [16,17]. Because of the high electron energy of 100 keV or more, the relative energy spread of the electron beam is small. Therefore, correction of the chromatic aberration is required only for further improvement of the resolution [18,19] or if the energy is strongly reduced like in a low voltage scanning electron microscope (LVSEM), where the resolution could be improved by a factor of 2 at 1 keV electron energy using a multipole corrector [20].

In contrast to TEM and SEM, LEEM uses an immersion objective lens, i.e. the electron energy is high in the image column (about 20 keV), but low (between 0 and 1000 eV) at the sample surface. The big advantage of low-energy electrons is the small inelastic mean-free path in the specimen of only 0.4–10 nm, rendering the instrument sensitive to only a few atomic layers. Furthermore, the low kinetic energy reduces the risk of beam

damage and allows studying *in-situ* and *real-time* surface processes even for hours without influencing the sample. However, a drawback of the low-energy range is the reduced lateral resolution, being one- to two-orders of magnitude poorer than in TEM or SEM. The reasons are the higher contributions of spherical and chromatic aberrations at low kinetic energy and the longer electron wavelength, which increases the diffraction limit. Whereas for kinetic energies below 10 eV the chromatic aberration dominates, the influence of both aberrations on the lateral resolution is comparable in size in the kinetic energy range of 10–1000 eV. Therefore, they have to be corrected simultaneously. A number of different concepts—time dependent fields [21–23] grid and foils in the electron path [24,25], numerical image reconstruction from a defocus series [26] and electron mirrors [27–29]—have been proven theoretically and experimentally capable for this purpose. However, up to now, the aberration correction in a LEEM or PEEM system could not yet successfully improve the lateral resolution.

2. Experimental

2.1. Influence of aberrations on the lateral resolution

In our LEEM/PEEM instrument, called SMART [30,31], we used an electrostatic tetrode electron mirror, attached to the system bench via a magnet deflector field. Over a wide range, the chromatic and spherical aberration coefficients C_c and C_s of the mirror can be varied separately by tuning three correlated voltages of the mirror electrodes and by a slight change of the field lens between the magnet deflector field and the mirror, where the focal length and the intermediate image position are set fixed. In the optimum case, the mirror and the objective lens aberration coefficients are the same, but with opposite sign. Starting with settings based on electron optical simulations, we optimized the optics with the help of experimental electron optical criteria suitable to measure quantitatively the residual spherical and chromatic aberrations.

In a simplified description, the lateral resolution limit d is determined by a Gaussian convolution of three contributions: $d^2 = d_d^2 + d_s^2 + d_c^2$, where $d_d = 0.61\lambda/\sin\alpha$ is the diffraction limit increasing with decreasing acceptance angle α , limited by the aperture in the back focal plane. Here $\lambda \cong \sqrt{1.5/E_0}$ is the electron wavelength in nm and E_0 denotes the kinetic electron energy in eV at the sample with respect to the vacuum level. d_s and d_c are the radii of the disks of confusion due to spherical and chromatic aberrations and can be expressed as a Taylor series expanded in terms of α and the relative energy spread $\kappa = \delta E/E_0$ (δE is the energy spread of the electron beam)

$$d_s = C_0\alpha + C_s\alpha^3 + C_{ss}\alpha^5 + \dots \quad (1)$$

$$d_c = C_c\kappa\alpha + C_{cc}\kappa^2\alpha + C_{cs}\kappa\alpha^3 + \dots \quad (2)$$

where C_0 denotes the defocus by the objective lens, whereas C_s and C_{ss} are the third- and fifth-order spherical aberration coefficients and C_c , C_{cc} and C_{cs} are the coefficients for the different ranks of the chromatic aberrations.

2.2. Determination of spherical aberration

For the experimental characterization and optimization process we took advantage of the narrow angular distribution (< 20 mrad at specimen) of the beam generated by the Schottky field emitter electron gun, which is sufficiently bright for short (< 1 s) acquisition time at highest magnification. Using a deflector in the illumination optics we scanned the angle α of

the specularly reflected beam at the sample over a wide range and observed the displacement d of an object in the image (see Fig. 1a). The angle was calibrated by the corresponding displacement in the diffraction plane: while the border of the Ewald sphere in the LEED corresponds to the full angular range ($\pm 90^\circ$), the shift of the specular spot with respect to the center is proportional to $\sin\alpha$. The displacement is caused by the spherical aberration: whereas a beam passing the lens near the axis is imaged into the correct plane, the off-axis beams are focused stronger and cross the optic axis between lens and image plane, leading to an image displacement. By tuning the electron mirror voltages to a non-compensating mode i.e., still imaging, but not introducing additional aberrations, we obtained the expected α^3 behavior of an uncorrected microscope (Fig. 1a, green curve). By changing the mirror settings we could even over-compensate the system (Fig. 1a, red curve). An intermediate setting resulted in the desired flat, i.e. corrected behavior (blue curve).

2.3. Determination of chromatic aberration

The correction of the chromatic aberration was demonstrated in a similar manner. Scanning solely the potential of the electron gun by ΔE around the base energy $E = 15$ keV (using a special power supply floating on the base voltage) varies the kinetic electron energy at the sample surface which is kept at constant potential. Since the special magnetic deflector field in the SMART is free of dispersion, it does not change the image quality. As a consequence, the image sharpness is only influenced by the chromatic aberration of the objective lens: in the uncorrected case the faster electrons are focused further away from the image plane. Therefore, as expected, the lens excitation has to be increased by ΔI to restore the sharpness (Fig. 1b, green curve). At a different corrector setting the lens current has to be reduced at increased energy (Fig. 1b, red curve) meaning overcompensation. The blue curve shows the desired flat behavior at an optimized setting.

The experimental data (square and triangular dots) in Fig. 1a can be fitted directly by Eq. (1); the resulting coefficients are presented in Table 1. The experimental data in Fig. 1b can be described by a simple second-order function

$$\Delta I = m_c\Delta E + m_{cc}\Delta E^2 \quad (3)$$

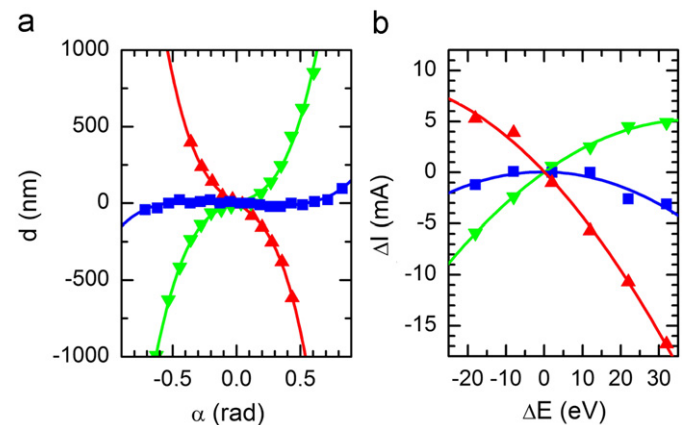


Fig. 1. Deflection d and defocus ΔI as effect of spherical (a) and chromatic (b) aberration for under-, well, and over-compensating mirror settings (green, blue, and red curves). The kinetic electron energy E_0 at the sample surface is 14 eV in (a). The sample potential in (b) is fixed to +17 eV referred to the base voltage (-15 kV) of the microscope, whereas the kinetic electron energy ΔE at the sample surface is varied by tuning the electron gun potential with respect to the base voltage. For interpretation of the references to colour in this figure legend, the reader is referred to the web version of this article.

Table 1

Spherical aberration coefficients C_s and C_{ss} and defocus C_0 resulting from the fits of the experimental data shown in Fig. 1a at different mirror settings C_c^{mirror} . The calculated spherical aberration of the objective lens is $C_s=5.7 \mu\text{m}$.

Correction state	Theoretical		Experimental		
	$C_c^{mirror}(\mu\text{m})$	$C_s(\mu\text{m})$	$C_0(\mu\text{m})$	$C_s(\mu\text{m})$	$C_{ss}(\mu\text{m})$
Overcompensated	16.3	-10.6	-0.55	-4.5	-
Compensated	8.2	-2.5	-0.06	0.15	0.16
Uncompensated	0.0	5.7	0.28	3.3	-

In order to extract the chromatic aberration coefficients from this fit, we describe the immersion objective lens as a superposition of an accelerating electric field, producing a virtual source image with a magnification $M_e=2/3$ (see for instance [32]), and a magnetic lens, with a magnification $M_m=b/g'$, the image and virtual source distance b and g' relative to the lens and an optical refraction power $D=D_e+D_m=1/f$ (f is the focal length, D_e and D_m the electrical and magnetic part of the refraction power). By means of an electron optical simulation program [33], using the boundary element method (BEM), it can be shown, that in the relevant working range $D_m=1/f_m=1/g'+1/b$ is well-described by the square of the excitation current $D_m \propto I^2$. Expanding the last two equations for small changes ΔD_m , one obtains, that a small change ΔI of the current causes an image shift Δb along the optical axis of

$$\Delta b = -2 \left(\frac{M}{M_e} + 1 \right) \frac{b}{I} \Delta I \quad (4)$$

with the total magnification of the objective lens of $M=M_e M_m$. Inserting the experimentally known values $b=235 \text{ mm}$, $I=1200 \text{ mA}$ and $M=18$ this simple formula yields $\Delta b/\Delta I = -11.0 \text{ mm/mA}$ which is in pretty agreement with the result of $\Delta b/\Delta I = -9.9 \text{ mm/mA}$ found with the BEM calculations.

In the image plane this shift causes a defocus by $d'_c = \Delta b \tan \alpha'$ with α' denoting the angular spread on the image side. The corresponding angular spread α on the surface is described by Snell's law and by the factor $1/M$ due to the image magnification

$$\frac{\sin \alpha'}{\sin \alpha} = \frac{1}{M} \sqrt{\frac{E_0}{E}} \quad (5)$$

where E_0 and E are the kinetic energy at the sample and at the image, respectively. This means for the defocus $d_c = d'_c/M$ on the image side for small α

$$\frac{d_c}{\alpha} = -\gamma \Delta I \text{ with } \gamma = 2 \left(\frac{M}{M_e} + 1 \right) \frac{b}{I} \frac{1}{M^2} \sqrt{\frac{E_0}{E}} \quad (6)$$

Inserting Eqs. (3) into (6) and comparing with Eq. (2) yields

$$C_c = \gamma E_0 m_c \text{ and } C_{cc} = \gamma E_0^2 m_{cc} \quad (7)$$

where the cubic term in Eq. (2) is neglected because $C_{cs} \alpha^2 / C_c < 1.6 \times 10^{-3}$ at the narrow beam divergence ($\alpha < 20 \text{ mrad}$) and $C_{cs}=11.6 \mu\text{m}$ and $C_c=2.8 \mu\text{m}$ calculated for the uncorrected case. Using Eq. (7), the fits of Fig. 1b lead to the coefficients summarized in Table 2. As Tables 1 and 2 show, the corrector clearly reduces the leading aberrations C_s and C_c by more than one-order of magnitude, which is sufficient to obtain a lateral resolution of less than 3 nm in both, LEEM and XPEEM if the residual defocus of the objective is set to $C_0 < 10 \text{ nm}$. The electron optical simulations (values in brackets) provide us with a trend but not values accurate enough to be used in the experimental procedure due to limited accuracy in the calculation and/or in the real geometry of the corrector. Therefore, the

Table 2

Chromatic aberration coefficients C_c and C_{cc} as experimentally derived from the fits shown in Fig. 1b at different mirror settings C_c^{mirror} . Theoretical values base on electron optical calculations with $C_c=2.8 \mu\text{m}$ for the objective lens.

Correction state	Theoretical		Experimental	
	$C_c^{mirror}(\mu\text{m})$	$C_c(\mu\text{m})$	$C_c(\mu\text{m})$	$C_c(\mu\text{m})$
Overcompensated	10.6	-7.8	-7.5	-1.37
Compensated	4.7	-1.9	0.06	-1.11
Uncompensated	0.0	2.8	5.2	-1.12

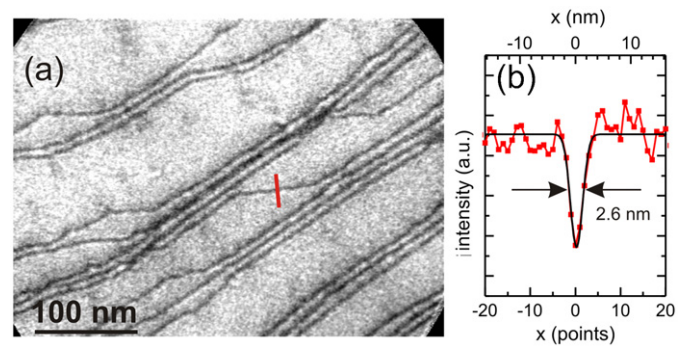


Fig. 2. Lateral resolution in LEEM (a) shows atomic steps on an Au(1 1 1) surface, $E_0=15 \text{ eV}$, FoV: $415 \times 307 \text{ nm}$, acquisition time $\Delta t=1 \text{ s}$. The Gaussian fit of the cross-section through a step (red line in (a)) reveals a lateral resolution of 2.6 nm. For interpretation of the references to colour in this figure legend, the reader is referred to the web version of this article.

optimum for the correction could only be found by using the criterion described above.

3. Results

With this aberration corrected optics, using an aperture setting of $\alpha=190 \text{ mrad}$ and an energy spread of $\Delta E=0.5 \text{ eV}$, we tested the lateral resolution at mono-atomic steps on the clean Au(1 1 1) surface (Fig. 2), which appears as dark lines due to Fresnel diffraction [1], using a kinetic electron energy nearly at out-of-phase condition for an atomic step on an Au(1 1 1) surface (the phase corresponds to $\phi=2.88\pi$). Here, the lateral resolution is directly estimated by the full-width of half maximum of the cross-section through a step, which corresponds to the well-known 14%/86% analysis in case of an amplitude contrast (rectangular-shaped contrast convoluted by the instrumental broadening) [34]. Even though for contrast enhancement the objective lens had to be tuned slightly out-of-focus [35], the cross-section demonstrates the best hitherto measured lateral resolution in LEEM of 2.6 nm, which is clearly better than the theoretical resolution limit of 4 nm predicted for an uncorrected LEEM system [36]. Up to now, the best experimental resolution claimed to be seen but without demonstrating the data has been 4.1 nm in an LEEM [37]. In XPEEM a lateral resolution of 22 nm has been shown [4]. The deviation of our experimental result from the theoretical optimum of 0.98 nm can be explained by some residual aberrations, the slight defocus, the non-optimal aperture size, but also by residual electric and mechanical instabilities.

The calibration of the image scaling is extremely important for the credibility of the lateral resolution. This is usually done either by theoretically calculating the overall magnification of the system or by direct experimental determination of the field of view (FoV). In the latter case, the mechanical movement of the sample manipulator can be directly related to the observed shift of the image features. Both methods were used with the SMART.

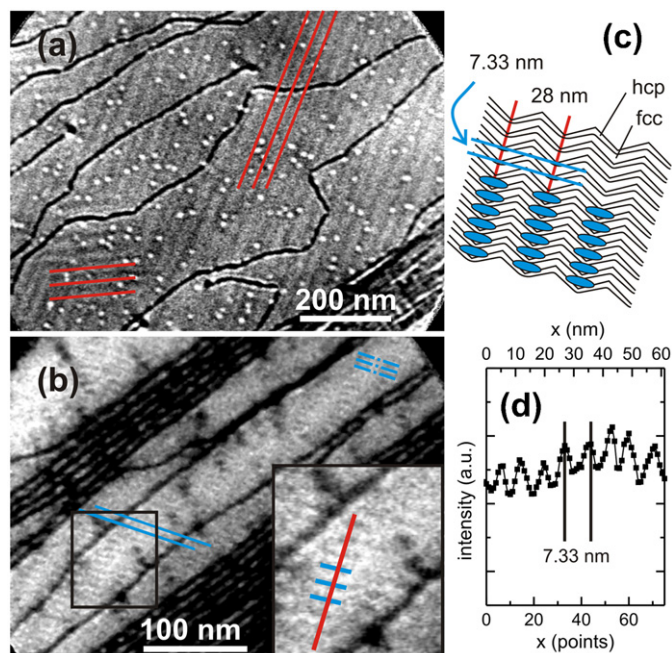


Fig. 3. Au(1 1 1) herringbone structure in LEEM: (a) and (b) are taken at $E_0=16$ and 15.3 eV, $\Delta t=5$ and 0.6 s, respectively, and at different magnifications. A model for the contrast is given in (c). (d) displays a cross-section along the red line in the inset of (b). For interpretation of the references to colour in this figure legend, the reader is referred to the web version of this article.

Additionally, as a highly precise calibration standard we used the Au(1 1 1)– $(22 \times \sqrt{3})$ herringbone reconstruction which is well documented in the literature with known periodicity [38].

The LEEM image in Fig. 3a shows large terraces on the Au(1 1 1) surface. In addition to the (dark) atomic steps and white dots due to carbon clusters—a striped pattern with weaker contrast is visible. Two directional domains can be identified: horizontal (in the lower left part) and rotated by 120° in the rest (see red lines as a guide for the eyes). These stripes go straight over nearly one micrometer and cross substrate steps without disruption, except for (screw-) dislocations (see bottom center). From this image a periodicity of 28 ± 0.5 nm can be estimated corresponding to the period in the herringbone structure (see model in Fig. 3c) found on large terraces [39]. A finer scale is the long axis of the $22 \times \sqrt{3}$ unit cell: with $d=22$ $a_0=6.35$ nm ($a_0=2.885$ Å being the atomic distance on the Au(1 1 1) surface). By rotating the direction by 120° a regular zig-zag pattern is formed, with a periodicity of $\delta=d/\cos 30^\circ=7.33$ nm perpendicular to the zig-zag lines (see Fig. 3c). This periodicity is found in Fig. 3b (see inset and cross-section in Fig. 3d). A simple model (Fig. 3c) might explain the contrast of these ripples. The elbows of the zig-zag lines separating fcc from hcp surface areas are not fully identical, one type has sharp 120° edges, whereas the other is pinched [39]. This leads to a larger fcc type area, indicated with blue marks. Therefore, the different electron reflectivity of the fcc and hcp structures causes the contrast in Fig. 3a and b. In Fig. 3a the individual blue marked areas are not resolved but washed out to stripes with 28 nm distance, whereas in Fig. 3b they appear as bunches of parallel and about 15 nm short dark lines. We used the distance of 7.33 nm between these lines as a precise standard to fine tune the scaling of the image Fig. 3b (and also in Fig. 2).

4. Conclusion

For the first time an electron microscope has proven that a double correction scheme for spherical as well as chromatic aberration using

a tetrode mirror successfully works and is able to visualize nanometer surface structures such as the herringbone reconstruction on the Au(1 1 1) surface, which are not accessible with uncorrected LEEM/PEEM instruments. With this corrector a lateral resolution of 2.6 nm has been demonstrated. Equipped with an imaging OMEGA-type energy analyzer the SMART is also operated as an XPEEM using photo-emitted core and valence level electrons and X-ray-excited secondary electrons. In this case, in addition to the expected improvement of lateral resolution, the transmission is enhanced by two-orders of magnitude, allowing much faster (time-resolved) imaging and lower specimen damage, a major advantage for spectroscopic investigations on sensitive samples.

Acknowledgement

The authors gratefully acknowledge the financial support by the Federal German Ministry of Education and Science (BMBF) under Contract 05 KS4WWB/4 and the technical support by the BESSY crew. The microscope is installed at the BESSY storage ring in Berlin.

References

- [1] E. Bauer, Rep. Prog. Phys. 57 (1994) 895–938.
- [2] E. Bauer, LEEM and SPLEEM, in: P Hawkes, J Spence (Eds.), Science of Microscopy, Springer, New York 2007, pp. 606–656.
- [3] A. Locatelli, E. Bauer, J. Phys. Condens. Matter 20 (2008) 093002.
- [4] Th. Schmidt, S. Heun, J. Slesak, J. Diaz, K.C. Prince, G. Lilienkamp, E. Bauer, Surf. Rev. Lett. 5 (1998) 1287–1296.
- [5] F.J. Meyer zu Heringdorf, M.C. Reuter, R.M. Tromp, Nature 412 (2001) 517–520.
- [6] Th. Schmidt, E. Bauer, Phys. Rev. B 62 (2000) 15815.
- [7] J.B. Hannon, R.M. Tromp, Annu. Rev. Mater. Res. 33 (2003) 263–288.
- [8] T. Duden, E. Bauer, Phys. Rev. Lett. 77 (1996) 2308–2311.
- [9] C.M. Schneider, G. Schönhense, Rep. Prog. Phys. 65 (2002) R1785–R1839.
- [10] J. Vogel, W. Kuch, M. Bonfim, J. Camarero, Y. Pennec, F. Offi, K. Fukumoto, J. Kirschner, A. Fontaine, S. Pizzini, Appl. Phys. Lett. 82 (2003) 2299–2301.
- [11] H.H. Rotermund, W. Engel, M. Kordes, G. Ertl, Nature 343 (1990) 355–357.
- [12] O. Scherzer, Z. Phys. 101 (1936) 593–603.
- [13] O. Scherzer, Optik 2 (1947) 114–132.
- [14] H. Rose, Sci. Technol. Adv. Mater. 9 (2008) 014107.
- [15] M. Haider, S. Uhlemann, E. Schwan, H. Rose, B. Kabius, K. Urban, Nature 392 (1998) 768–769.
- [16] O.L. Krivanek, N. Dellby, A.R. Lupini, Ultramicroscopy 78 (1999) 1–11.
- [17] B. Freitag, S. Kujawa, P.M. Mul, J. Ringnalda, P.C. Tiemeijer, Ultramicroscopy 102 (2005) 209–214.
- [18] C. Kisielowski, et al., Microsc. Microanal. 14 (2008) 469–477.
- [19] R. Erni, M.D. Rossell, C. Kisielowski, U. Dahmen, Phys. Rev. Lett. 102 (2009) 096101.
- [20] J. Zach, M. Haider, Nucl. Instrum., Methods Phys. Res. A 365 (1995) 316–325.
- [21] C. Oldfield, J. Phys. E 9 (1976) 455–463.
- [22] I. Dietrich, K.H. Herrmann, C. Passow, Optik 42 (1975) 439–462.
- [23] G. Schönhense, H. Spiecker, J. Vac. Sci. Technol. B 20 (2002) 2526–2534.
- [24] M. Hibino, S. Maruse, J. Electron Microsc. 25 (1976) 229–236.
- [25] H. Matsuda, H. Daimon, M. Kato, M. Kudo, Phys. Rev. E 71 (2005) 066503.
- [26] T. Koshikawa, H. Shimizu, R. Amkawa, T. Ikuta, T. Yasue, E. Bauer, J. Phys. Condens. Matter 17 (2005) S1371–S1380.
- [27] G.F. Rempfer, M.S. Mauck, Optik 92 (1992) 3–8.
- [28] H. Rose, D. Preikszas, Optik 92 (1992) 31–44.
- [29] H. Rose, D. Preikszas, Nucl. Instrum., Methods Phys. Res. A 363 (1995) 301–315.
- [30] R. Fink, et al., J. Electron Spectrosc. Relat. Phenom. 84 (1997) 231–250.
- [31] Schmidt Th., et al., Surf. Rev. Lett. 9 (2002) 223–232.
- [32] H. Liebl, Applied Charged Particle Optics, Springer, Berlin Heidelberg, 2008, p. 20.
- [33] D. Preikszas, P. Hartel, R. Spehr, H. Rose, in: Proceedings of the EUREM 12, Brno, Czech Republic, July 9–14, 2000, p. 181.
- [34] M.S. Altman, J. Phys.: Condens. Matter 22 (2010) 084017.
- [35] W.F. Chung, M.S. Altman, Ultramicroscopy 74 (1998) 237–246; A.B. Pang, Th. Müller, M.S. Altman, E. Bauer, J. Phys.: Condens. Matter 21 (2009) 314006.
- [36] R.M. Tromp, M. Mankos, M.C. Reuter, A.W. Ellis, M. Copel, Surf. Rev. Lett. 5 (1998) 1189–1197.
- [37] R.M. Tromp, J.B. Hannon, A.W. Ellis, W. Wan, A. Berghaus, O. Schaff, Ultramicroscopy 110 (2010) 852–861.
- [38] J.V. Barth, H. Brune, G. Ertl, R.J. Behm, Phys. Rev. B 42 (1990) 9307–9318.
- [39] D.D. Chambliss, R.J. Wilson, S. Chiang, J. Vac. Sci. Technol. B 9 (1991) 933–937.